RSC Advances

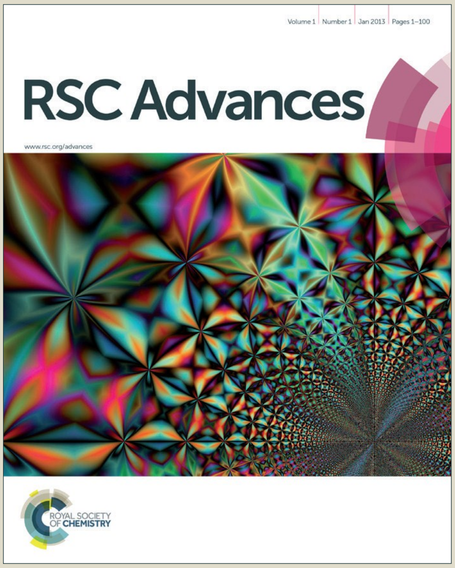

ROYAL SOCIETY OF CHEMISTRY

www.rsc.org/advances

Organic-inorganic hybrid perovskites ABI_3 (A = CH_3NH_3, NH_2CHNH_2; B = Sn, Pb) as potential thermoelectric materials: A density functional evaluation

Changhoon Lee[1,2], Jisook Hong[1], Alessandro Stroppa[3], Myung-Hwan Whangbo[2*], and Ji Hoon Shim[1,4]*

[1] Department of Chemistry, Pohang University of Science and Technology, Pohang 790-784, Korea

[2] Department of Chemistry, North Carolina State University, Raleigh, North Carolina 27695-8204, USA

[3] Consiglio Nazionale delle Ricerche - CNR-SPIN, I-67100 L'Aquila, Italy

[4] Division of Advanced Nuclear Engineering, Pohang University of Science and Technology, Pohang 790-784, Korea

Keywords: Organic-inorganic hybrid perovskites, Thermoelectric properties, Density functional calculations

Abstract

To assess the feasibility of the organic-inorganic perovskite iodides ABI_3 (A = CH_3NH_3, NH_2CHNH_2; B = Sn, Pb; X = I) for thermoelectric applications, we estimated their figures of merit (ZTs) as well as that of Bi_2Te_3, which is optimized for temperatures around 300 K, as a function of chemical potential on the basis of density functional theory calculations. Our analysis employed the tetragonal structures (P4mm) of $(CH_3NH_3)PbI_3$ and $(CH_3NH_3)SnI_3$, the trigonal (P3m1) structure of $(NH_2CHNH_2)PbI_3$, and the orthorhombic (Amm2) structure of $(NH_2CHNH_2)SnI_3$ to examine their thermoelectric properties around room temperature. Our work reveals that the ZTs of electron-doped ABI_3 perovskites can be as large as that of hole-doped Bi_2Te_3 whereas those of hole-doped ABI_3 are rather smaller so that, in thermoelectric performance, electron-doped perovskites ABI_3 can be as good as hole-doped Bi_2Te_3.

1. Introduction

In organic-inorganic hybrid perovskite iodides ABI_3 (A = CH_3NH_3, NH_2CHNH_2; B = Sn, Pb), BI_6 octahedra containing divalent cations B^{2+} form a three-dimensional (3D) perovskite lattice BI_3. The monovalent cations A^+ such as methyl ammonium (MA), $CH_3NH_3^+$, or formamidinium (FA), $NH_2CHNH_2^+$, occupy the center of each B_8 cube made up of eight corner-sharing BI_6 octahedra. These perovskites have been examined as light harvesting materials,[1,2] solar-cell absorbers,[3-6] and the tunability of the ferroelectric properties.[7] They were also considered as new n-type thermoelectric materials[8-10] and as solar thermoelectric generators, an alternative to thermoelectric devices.[11-13] The efficiency of thermoelectric energy conversion is measured by the figure of merit, $ZT = (S^2\sigma/\kappa)T$, where S, σ, κ, and T refer to the Seebeck coefficient, electrical conductivity, thermal conductivity, and temperature, respectively.[14] Efficient thermoelectric materials need to possess a relatively large value of the power factor, $S^2\sigma$, and a low thermal conductivity $\kappa = \kappa_e + \kappa_L$, where κ_e is the electron thermal conductivity arising from charge carriers, and κ_L is the lattice thermal conductivity. In general, κ_e increases with increasing σ, so that κ_L is expected to be more important in controlling the ZT. Electronic structure calculations for ABI_3 perovskites show that, as expected, they all have a band gap.[8,15-17] However, as-grown samples of $(MA)SnI_3$ were reported to exhibit metallic properties due to a trace amount of spontaneous hole-doping in the crystallization process.[15] A systematic investigation revealed that samples of ABI_3 perovskites behave as p- or n-type semiconductors depending on the preparation method, and n-type samples have a low carrier concentration.[9] The lattice thermal conductivity of $(MA)PbI_3$ was found to be very low.[18]

Very recently, He and Galli[10.b] evaluated the thermoelectric properties of $(MA)BI_3$ (B = Pb, Sn) using the Kane single band model[19] on the basis of DFT calculations. Their results show that the maximum ZT values of these compounds can be obtained from electron doping rather than from hole doping. In their evaluation of the thermal transport coefficients, they calculated the electrical mobility μ by considering only the acoustic phonon scattering (electron–phonon interaction). There are several factors governing the electrical mobility. According to Matthiessen's rule, the actual mobility μ_e is written as

$$\frac{1}{\mu_e} = \frac{1}{\mu_{\text{acoustic phonon}}} + \frac{1}{\mu_{\text{optical phonon}}} + \frac{1}{\mu_{\text{impurity}}} + \cdots. \quad (1)$$

To know the actual mobility μ_e, we need to consider various contributions such as acoustic phonons, optical phonons, impurities and surface scattering. In typical semiconducting materials, it is known that ionized impurities and acoustic phonons are important scattering sources. Especially in heavily doped semiconductor, there would be more ionized impurities so their scattering would be more important. In addition, when there are more than 10^{17} electrons per cm^3, electron-electron scattering starts to become significant. He and Galli considered only the acoustic phonon scattering in the doping range $1\times10^{16} – 5\times10^{19}$ cm^{-3} so their estimate of the mobility might be much larger than the actual mobility of the material, leading an overestimated relaxation time τ (see Eq. 2).

$$\mu_e = e\tau/m^* \qquad (2)$$

where e, and m* are the electric charge and effective mass, respectively.

In the present work we assess the feasibility of the perovskite iodides the ABI_3 for thermoelectric applications by evaluating the power factor (PF), $S^2\sigma$, and the figure of merit, $ZT = (S^2\sigma/\kappa)T$, as a function of the chemical potential (equivalently, as a function of charge carrier density) on the basis of density functional theory (DFT) calculations. For this purpose, it is necessary to calculate the thermoelectric properties of these perovskites using their crystal structures around room temperature, and compare them with those of the well-known thermoelectric material Bi_2Te_3 that is optimized for temperatures around 300 K.[20,21] The structures of the perovskites ABI_3 depend on temperature, because the organic cations A^+ rattle around within their B_8 cages interacting with the BI_3 framework.[15, 22-24]. Thus, we examine the tetragonal structures (P4mm) of $(MA)PbI_3$ and $(MA)SnI_3$, the trigonal (P3m1) structure of $(FA)PbI_3$, and the orthorhombic (Amm2) structure of $(FA)SnI_3$ (**Table 1**).[8] Experimentally, the precise atomic positions of these perovskite iodides are poorly determined (particularly, those of the organic cations) so that we first optimize the atomic positions of these crystal structures by DFT calculations and then use the optimized structures to calculate their thermoelectric properties. Our work suggests that, in their thermoelectric efficiency, the iodide perovskites ABI_3 can be nearly as good as that of Bi_2Te_3 if enough electrons can be doped. Under hole doping, they are not expected to be as efficient as Bi_2Te_3.

2. Theoretical aspects and computational details

For a semiconductor, the band gap E_g is given by $E_g = E_{CBM} – E_{VBM}$, where E_{CBM} and E_{VBM} refer to the energies of the conduction band minimum (CBM) and valence band maximum (VBM), respectively. The chemical potential μ for holes ($\mu < 0$) is defined as $\mu = E – E_{VBM}$ where $E < E_{VBM}$, and that for electrons ($\mu > 0$) by $\mu = E – E_{CBM}$ where $E > E_{CBM}$. The charge carriers available for a hole-doped or an electron-doped semiconductor at a given chemical potential μ can be approximated by integrating the electronic density of states (DOS) N(μ).

Our DFT electronic structure calculations employed the frozen-core projector augmented wave (PAW) method[25] encoded in the Vienna *ab initio* simulation package (VASP) [26] using the generalized-gradient approximation (GGA)[27] of Perdew, Burke and Ernzerhof for the exchange-correlation functional with the plane-wave-cut-off energy of 550 eV, the Monkhorst-Pack k-points mesh of 10×10×10, and the threshold of self-consistent-field energy convergence of 10^{-6} eV. In general, it is not easy to measure exact positions of small atoms such as hydrogen atoms by XRD measurements. For this reason, the hydrogen atom positions of organic molecules are not specified in most cases. Thus, we add H atoms to the FA and MA molecules and then optimize the atom positions of ABI_3 while keeping constant the cell parameters ABI_3 on the basis of density functional calculations. The atomic positions of $(MA)PbI_3$, $(MA)SnI_3$, $(FA)PbI_3$, and $(FA)SnI_3$ were fully optimized until all the residual forces are smaller than 0.005 eV/Å with their cell parameters fixed (**Table 1**). The atom positions obtained from these optimizations are summarized in **Table S1-S4** of the supporting information (SI). Heavy elements such as Pb, Sn and I possess a strong spin orbit coupling (SOC) effect. We examine the SOC effect on our calculations by comparing the band gaps of the perovskite iodides obtained from GGA and GGA+SOC calculations. As listed in **Table 2**, the band gaps determined from the GGA calculations agree better with the experimental band gaps than do those from the GGA+SOC calculations, as has already been reported for $(MA)PbI_3$.[16] In estimating thermoelectric properties, it is important to describe a band gap correctly so that our discussion of the perovskite iodides will be based on GGA calculations.

The thermoelectric properties of all considered ABI_3 systems were calculated by using the BoltzTrap code,[28] which solves the semi-classical Boltzmann equation using the rigid band approach [29] under the constant relaxation time approximation. The electronic structures of ABI_3 needed for these calculations were obtained by performing GGA calculations with the Monkhorst-Pack k-points mesh of 15×15×15. We calculate the Seebeck coefficients (S), the electrical conductivity (σ), the electric thermal conductivity (κ_e), the power factor $S^2\sigma$ under the assumption that the total electron momentum relaxation time τ is independent of energy. The latter approximation, though simple, has provided explanations for the thermoelectric properties of numerous systems.[30-34]

3. Electronic structures

The band dispersion relations calculated for $(MA)PbI_3$, $(MA)SnI_3$, $(FA)PbI_3$, and $(FA)SnI_3$ are summarized in **Fig. 2**. $(FA)PbI_3$ and $(FA)SnI_3$ have a direct band gap at (0.5, 0, 0), while $(MA)PbI_3$ and $(MA)SnI_3$ have a direct band gap at R = (0.5, 0.5, 0.5). In cubic ABI_3 perovskites, a direct band gap occurs at R = (0.5, 0.5, 0.5).[17] The low-temperature distorted phases of ABI_3 do not differ much from their high temperature cubic phases so that the electronic structures of the low-temperature distorted ABI_3 are quite similar to those of their high-temperature cubic structures. Thus, the direct band gap opens at R for $(MA)BI_3$ (B = Pb, Sn). The occurrence of a direct band gap at (0.5, 0, 0) for the low-temperature $(FA)BI_3$ arises from the increase in the unit cell size caused by the structural distortion and the concomitant folding of the Billouin zone. The calculated band gaps of $(MA)PbI_3$ and $(FA)PbI_3$ are greater than those of their Sn analogues. The calculated band gaps obtained from our GGA (GGA+SOC) calculations are 1.69 (1.12), 1.62 (0.91), 0.86 (0.78), and 0.74 (0.75) eV for $(MA)PbI_3$, $(FA)PbI_3$, $(MA)SnI_3$, and $(FA)SnI_3$, respectively. The experimentally observed band gaps are 1.55, 1.48, 1.35, and 1.41 for (MA)PbI_3,[35] (FA)PbI_3,[36] (MA)SnI_3,[8] and (FA)SnI_3,[37] respectively.

The total DOS and projected DOS plots calculated for (MA)PbI_3, (MA)SnI_3, (FA)PbI_3, and (FA)SnI_3 are presented in **Fig. 3.** The VBM is composed of the Pb 6s and I 5p states for (MA)PbI_3 and (FA)PbI_3, and the Sn 5s and I 5p states for (MA)SnI_3 and (FA)SnI_3. The CBM is made up of the Pb 6p states for (MA)PbI_3 and (FA)PbI_3, and the Sn 5p states for (MA)SnI_3 and (FA)SnI_3. At the VBM, the Pb 6s - I 5p antibonding is weaker than the Sn 5s - I 5p antibonding, most likely because the Pb-O bonds are longer than the Sn-O bonds and because Pb 6s orbital is more diffuse than the Sn 5s orbital. The organic cations A^+ of the perovskites ABI_3 have their filled states well below the VBM, their empty states well above the CBM, and their contribution to the Fermi level is very weak. Thus, the transport properties of ABI_3 are governed by the electrons or holes generated in the BI_3 framework. The important role of the A^+ cations is that, by rattling within the B_8 cages, the A^+ cations would disturb the acoustic phonon dispersions of the BI_3 framework and hence lower the lattice thermal conductivity κ_L, as found for the rattling cations of Skutterudites in their cages.[38]

4. Thermoelectric properties

We now compare the calculated thermoelectric properties of ABI_3 compounds with those of a p-type semiconductor Bi_2Te_3. The Seebeck coefficients S of ABI_3 calculated as a function of the chemical potential μ are shown in **Fig. 4a**, which exhibits two peaks at $\mu \approx +0.1$ and -0.1 eV. At 400 K the maximum Seebeck coefficients are ~1600 μV/K for (MA)PbI_3 and (FA)PbI_3, and ~800 μV/K for (MA)SnI_3 and (FA)SnI_3. The Seebeck coefficients are considerably larger for the Pb systems because they have narrower band dispersions around the Fermi level and a larger band gap than do the Sn systems. The Seebeck coefficients of the ABI_3 perovskites are quite large compared with that of Bi_2Te_3 because the perovskites have a much larger band gap than does Bi_2Te_3 (E_g = 0.21 eV for Bi_2Te_3). In general, the electron momentum relaxation time τ of conventional semiconductors is of the order of 10^{-14} s.[20,21,39,40] For example, τ ≈ 2×10^{-14} and 3×10^{-14} s have been reported to reproduce the experimental resistivities of Bi_2Te_3 and PbTe, respectively.[20,21,40] Thus, in calculating the electron conductivity σ and hence the power factor $S^2\sigma$ for all the ABI_3 perovskites and Bi_2Te_3, we employed $\tau = 2\times10^{-14}$ s for direct comparison of their transport properties. Indeed, the calculated electronic conductivities at low carrier concentrations show a good agreement with the experimentally observed values for $(MA)SnI_3$ [18] and $(MA)PbI_3$.[10a] The dependence of the power factor $S^2\sigma$ on the chemical potential μ is presented in **Fig. 4b**, which exhibits maximum peaks around μ ≈ 0.8 eV with values slightly larger for the $ASnI_3$ than for the $APbI_3$ perovskites. The maximum $S^2\sigma$ values of ABI_3 are ~0.007 $WK^{-2}m^{-1}$ at 400 K, which can be achieved by electron doping. On the other hand, the maximum $S^2\sigma$ value attainable by hole doping is an order of magnitude smaller than that attainable by electron doping as well as that of Bi_2Te_3. In terms of $S^2\sigma$ alone, the perovskites ABI_3 would be expected to be a poor thermoelectric material compared to Bi_2Te_3 (**Fig. 4b**). However, what matters for thermoelectric properties is the figure of merit $ZT = (S^2\sigma/\kappa)T$, which can be enhanced by reducing the value of the thermal conductivity $\kappa = \kappa_L + \kappa_e$.

The electron thermal conductivities κ_e calculated for ABI_3 and Bi_2Te_3 as a function of μ at 400 K are presented in **Fig. 4c**. The lattice thermal conductivities κ_L measured for single crystal and polycrystalline samples of $(MA)PbI_3$ are 0.5 and 0.3 $WK^{-1}m^{-1}$, respectively.[19] For Bi_2Te_3, the reported the lattice thermal conductivities is κ_L = 1.2 $WK^{-1}m^{-1}$.[20,21] Indeed, the simulated ZT value for Bi_2Te_3 well describes the experimentally measured one with κ_L = 1.2 $WK^{-1}m^{-}1$ and $\tau = 2\times10^{-14}$ s. Although the measured lattice thermal conductivity of $(MA)PbI_3$ is 0.5 $WK^{-1}m^{-1}$, we adopt κ_L = 1.2 $WK^{-1}m^{-1}$ for ABI_3 and Bi_2Te_3 for direct comparison of their thermoelectric properties in estimating the ZT values for ABI_3 and Bi_2Te_3 at 400 K. The ZTs at 400 K calculated for ABI_3 and Bi_2Te_3 as a function of μ are presented in **Fig. 4d**. It is noted that the optimum ZTs of ABI_3 in the $\mu > 0$ (electron-doped) region are comparable to that of Bi_2Te_3 in the $\mu < 0$ (hole-doped) region. In conventional semiconducting materials, the optimum ZT is generally found for the carrier concentration around $10^{19} – 10^{20}$ cm^{-3}.[41] Indeed, around the chemical potential $\mu \approx 0.4$ and 0.8 eV, leading to the optimum ZTs of $ASnI_3$ and $APbI_3$, the DOS value $N(\mu)$ corresponds to the carrier concentration around $10^{19} – 10^{20}$ cm^{-3}. In **Fig. 4d**, the values of the optimal carrier concentration for each compound are indicated in the unit of 10^{19} cm^{-3}. It should be noted that, in the $\mu < 0$ (hole-doped) region, the optimum ZTs of ABI_3 are considerably smaller than that of Bi_2Te_3. Thus, only when they are electron doped, the perovskites would be as good a thermoelectric material as Bi_2Te_3. As already pointed out in introduction section, He and Galli [10b] evaluated the thermoelectric properties of $(MA)BI_3$ (B = Pb, Sn) on the basis of DFT calculations using the Kane single band model.[19] Their study also shows that the maximum ZT values of these compounds can be obtained from electron doping rather than from hole doping. However, their ZT values are optimized with the carrier concentration of $\sim 10^{18}$$cm^{-3}$, due to the use of an overestimated value for the mobility. It should lead to an extreme overestimation of the relaxation time τ as a result. We calculated the ZT values of $(MA)PbI_3$ system by adopting various relaxation times τ to see how the relaxation time affects the ZT values as shown in Fig. S2, which shows the ZT values to be strongly influenced by the relaxation time τ. Our work suggests that the carrier concentration of $10^{19} \sim 10^{20}$ cm^{-3} is needed for the optimum ZT values (see Fig. S3).

5. Concluding remarks

The thermoelectric properties of the perovskite iodides ABI_3 were compared with that of

Bi_2Te_3 on the basis of DFT calculations. The ZTs of the electron-doped ABI_3 can be as large as that of hole-doped Bi_2Te_3 while those of hole-doped ABI_3 are rather smaller. Thus, electron-doped perovskites ABI_3 are expected to exhibit as good a thermoelectric performance as does hole-doped Bi_2Te_3. Experimentally, it is known that the carrier density is rather low in electron-doped ABI_3 perovskites. It would be an interesting challenge to see if ABI_3 perovskites can be doped with a large number of electrons.

Supporting information

Tables S1 – S4 and **Figures S1 – S3** are available free of charge via the Internet at http://

Acknowledgements

This research was supported by Global Frontier Program through the Global Frontier Hybrid Interface Materials (GFHIM) of the National Research Foundation of Korea (NRFK) funded by the Ministry of Science, ICT & Future Planning (2013M3A6B1078870) and by the resource of Supercomputing Center/Korea Institute of Science and Technology Information with supercomputing resources including technical support (KSC-2014-C1-024 and KSC-2014-C1-52). This research was supported by the computing resources of the NERSC center and the HPC center of NCSU.

References

1 J. Burschka, N. Pellet, S. –J. Moon, R. Humphry-Baker, P. Gao, M. K. Nazeeruddin and M. Grätzel, *Nature*, 2013, **499**, 316-319.

2 H. J. Snaith, *J. Phys. Chem. Lett.*, 2013, **4**, 3623-3630.

3 M. A. Green, A. Ho-Baillie and H. J. Snaith, *Nat. Photonics*, 2014, **8**, 506–514.

4 M. M. Lee, J. Teuscher, T. Miyasaka, T. N. Murakami and H. J. Snaith, *Science*, 2012, **338**, 643-647.

5 A. Kojima, K. Teshima, Y. Shirai and T. Miyasaka, *J. Am. Chem. Soc.*, 2009, **131**, 6050-6051.

6 L. Etgar, P. Gao, Z. Xue, Q. Peng, A. K. Chandiran, B. Liu, M. K. Nazeeruddin and M. Gratzel, *J. Am. Chem. Soc.*, 2012, **134**, 17396-17399.

7 Stroppa, A.; Di Sante, D.; Barone, P.; Bokdam, M.; Kresse, G.; Franchini, C.; Whangbo, M.-H. Picozzi, S. *Nature Comm*., 2014, **5**, 3335-3339.

8 C. C. Stoumpos, C. D. Malliakas and M. G. Kanatzidis, *Inorg. Chem*., 2013, **52**, 9019-9038.

9 F. Hao, C. C. Stoumpos, D. H. Cao, R. P. H. Chang and M. G. Kanatzidis, *Nat. Photonics.*, 2014, **8**, 489-494.

10 (a) X. Mettan, R. Pisoni, P. Matus, A. Pisoni, J. Jaćimović, B. Náfrádi, M. Spina, D. Pavuna, L. Forró and E. Horváth, *Phys. Chem. C*, 2015, **119**, 11506–11510. (b) Y. He and G. Galli, *Chem. Mater*., 2014, **26**, 5394-5400.

11 D. Kraemer, B. Poudel, H. –P. Feng, J. C. Caylor, B. Yu, X. Yan, Y. Ma, X. Wang, D. Wang, A. Muto, K. McEnaney, M. Chiesa, Z. Ren and G. Chen, *Nat. Mater*., 2011, **10**, 532-538.

12 L. L. Baranowski, G. J. Snyder and E. S. Toberer, *Energy Environ. Sci*., 2012, **5**, 9055-9067.

13 W. –H. Chen, C. –C. Wang, C. –I. Hung, C. –C. Yang and R. –C. Juang, *Energy*, 2014, **64**, 287-300.

14 G. S. Nolas, J. Sharp and H. J. Goldsmid, *Thermoelectrics-Basic principles and New Materials Developments*, Springer, Berlin, 2001.

15 (a) Y. Takahashi, R. Obara, Z. –Z. Lin, Y. Takahashi, T. Naito, T. Inabe, S. Ishibashi and K. Terakura, *Dalton Trans.*, 2011, **40**, 5563-5568; (b) Y. Takahashi, H. Hasegawa, Y. Takahashi and T. Inabe, *J. Solid State Chem.*, 2013, **205**, 39-43.

16 E. Menéndez-Proupin, P. Palacios, P. Wahnón and J. C. Conesa, *Phys. Rev. B*, 2014, **90**, 045207.

17 L. Li, J. Yang, H. Liu, H. J. Xiang and X. G. Gong, *Phys. Lett.* A, 2014, **378**, 290-293.

18 A. Pisoni, J. Jaćimović, O. S. Barišić, M. Spina1, R. Gaál1, L. Forró1 and E. Horváth, *J. Phys. Chem. Lett.*, 2014, **5**, 2488-2492.

19 Y. I. Ravich, B. A. Efimova and I. A. Smirnov, *Semiconducting Lead Chalcogenides*, Plenum Press, New York, 1970, p. 85−216.

20 (a) H. –W. Jeon, H. –P. Ha, D. –B. Hyun and J. –D. Shim, *J. Phys. Chem. Solids*, 1991, **52**, 579-587; (b) T. J. Scheidemantel, C. Ambrosch-Draxl, T. Thonhauser, J. V. Badding and J. O. Sofo, *Phys. Rev. B*, 2003, **68**, 125210.

21 B. –L. Huang and M. Kaviany, *Phys. Rev. B*, 2008, **77**, 125209.

22 D. B. Mitzi and K. Liang, *J. Solid State Chem.*, 1997, **134**, 376-381.

23 A. Poglitsch and D. Weber, *J. Chem. Phys.*, 1987, **87**, 6373–6378.

24 T. Baikie, Y. N. Fang, J. M. Kadro, M. Schreyer, F. X. Wei, S. G. Mhaisalkar, M. Graetzel and T. J. White, *J. Mater. Chem. A*, 2013, **1**, 5628–5641.

25 (a) P. E. Blöchl, *Phys. Rev. B*, 1994, **50**, 17953-17979; (b) G. Kresse and D. Joubert, *Phys. Rev. B*, 1999, **59**, 1758-1775.

26 G. Kresse and J. Furthmüller, *Phys. Rev. B*, 1996, **54**, 11169-11186.

27 J. P. Perdew, K. Burke and M. Ernzerhof, *Phys. Rev. Lett.*, 1996, **77**, 3865-3868.

28 G. K. H. Madsen and D. J. Singh, *Comp. Phys. Commun.*, 2006, **175**, 67-71.

29 T. Boker, R. Severin, A. Muller, C. Janowitz, R. Manzke, D. Vob, P. Kruger, A. Mazur and J. Pollmann, *Phys. Rev. B*, 2001, **64**, 235305.

30 (a) K. P. Ong, D. J. Singh and P. Wu, *Phys. Rev. B*, 2011, **83**, 115110; (b) D. Parker, M. –H. Du and D. J. Singh, *Phys. Rev. B*, 2011, **83**, 245111; (c) L. Zhang and D. J. Singh, *Phys. Rev. B*, 1993, **47**, 13164-13174. (d) D. J. Singh, *Phys. Rev. B*, 2010, **81**, 195217; (e) L. Zhang, M. -H. Du and D. J. Singh, *Phys. Rev. B*, 2010, **81**, 075117; (f) G. K. H. Madsen, K. Schwarz, P. Blaha and D. J. Singh, *Phys. Rev. B*, 2003, **68**, 125212; (g) T. J. Scheidemantel, C. Ambrosch-Draxl, T. Thonhauser, J. V. Badding and J. O. Sofo, *Phys. Rev. B*, 2003, **68**, 125210; (h) L. Bertini and C. Gatti, *J. Chem. Phys.*, 2004, **121**, 8983-8989; (i) L. Lykke, B. B. Iversen and G. K. H. Madsen, *Phys. Rev. B*, 2006, **73**, 195121; (j) Y. Wang, X. Chen, T. Cui, Y. Niu, Y. Wang, M. Wang, Y. Ma and G. Zou, *Phys. Rev. B*, 2007, **76**, 155127; (k) B. Xu, C. G. Long, Y. Wang and L. Yi, *Chem. Phys. Lett.*, 2012, **529**, 45-51; (l) H. A. Rahnamaye Aliabad, M. Ghazanfari, I. Ahmad and M. A. Saeed, *Comp. mater. Sci.*, 2012, **65**, 509-519; (m) C. Lee, J. Hong, M. –H. Whangbo and J. H. Shim, *Chem. Mater.*, 2013, **25**, 3745-3752; (n) C. Lee, J. Hong, W. R. Lee, D. Y. Kim and J. H. Shim, *J. Solid State Chem.*, 2014, **211**, 113-119.

31 T. J. Scheidemantel, C. Ambrosch-Draxl, T. Thonhauser, J. V. Badding and J. O. Sofo, *Phys. Rev. B*, 2003, **68**, 125210.

32 G. K. H. Madsen, *J. Am. Chem. Soc.*, 2006, **128**, 12140-12146.

33 L. Chaput, P. Pécheur, J. Tobola and H. Scherrer, *Phys. Rev. B*, 2005, **72**, 085126.

34 X. Gao, K. Uehara, D. D. Klug, S. Patchkovskii, J. S. Tse and T. M. Tritt, *Phys. Rev. B*, 2005, **72**, 125202.

35 (a) J. H. Noh, S. H. Im, J. H. Heo, T. N. Mandal and S. I. Seok, *Nano Lett.*, 2013, **13**, 1764–1769; (b) H. S. Jung and N. –G. Park, *Small*, 2015, **11**, 10-25.

36 G. E. Eperon, S. D. Stranks, C. Menelaou, M. B. Johnston, L. M. Herz and H. J. Snaith, *Energy Environ. Sci.*, 2014, **7**, 982-988.

37 W. Yin, J. Yang, J. Kang, Y. Yan and S. –H. Wei, DOI: 10.1039/c4ta05033a.

38 (a) W. Jeitschko and D. J. Braun, *Acta Crystallogr. Sect. B*, 1977, **33**, 3401-3406; (b) B. C. Sales, D. Mandrus and R. K. Williams, *Science*, 1996, **272**, 1325-1328; (c) B. C. Sales, D. Mandrus, B. C. Chakoumakos, V. Keppens and J. R. Thompson, *Phys. Rev. B*, 1997, **56**, 15081-15089.

39 (a) J. –S. Rhyee, K. H. Lee, S. M. Lee, E. Cho, S. I. Kim, E. Lee, Y. S. Kwon, J. H. Shim and G. Kotliar, *Nature*, 2009, **459**, 965-968; (b) H. S. Ji, H. Kim, C. Lee, J. –S. Rhyee. M. H. Kim, M. Kaviany and J. H. Shim, *Phys. Rev. B*, 2013, **87**, 125111.

40 S. Ahmad and S. D. Mahanti, *Phys. Rev. B*, 2010, **81**, 165203.

41 G. Mahan, B. Sales and J. Sharp, *Phys. Today*, 1997, **50**, 42-47.

Figure captions

Figure 1. Schematic projection views of organic-inorganic hybrid perovskites along the c-axis: (a) (MA)BI_3 and (b) (FA)BI_3, where M = Pb, Sn. MA = methyl ammonium ($CH_3NH_3^+$), and FA = formamidinium ($HC(NH_2)_2^+$). The blue, grey and black circles represent the N, C and H atoms, respectively, and purple octahedral units represent the BI_6 octahedra. The C-N axis of MA and the N…N axis of FA cations are oriented along the c-axis, but are shown schematically to show their chemical structures.

Figure 2. Band dispersion relations calculated for (a) (MA)PbI_3, (b) (MA)SnI_3, (c) (FA)PbI_3, and (d) (FA)SnI_3. They were calculated along the high symmetry lines Γ-X-M-Γ-R for (MA)PbI_3, (MA)SnI_3, and (FA)SnI_3, where Γ = (0, 0, 0), X = (1/2, 0, 0), M = (1/2, 1/2, 0), and R = (1/2, 1/2, 1/2) in the first Brillouin zone (Fig. S1 of the SI). For (FA)PbI_3, the band structures were calculated along the high symmetry lines Γ-M-K-Γ-H, where Γ = (0, 0, 0), M = (1/2, 0, 0), K = (1/3, 1/3, 0), and H = (1/3, 1/3, 1/2) in the first Brillouin zone (Fig. S1 of the SI).

Figure 3. The calculated total DOS of ABI_3 (left) and projected DOS of BI_3 (right): (a) (MA)PbI_3, (b) (MA)SnI_3, (c) (FA)PbI_3, and (d) (FA)SnI_3. In the total DOS, the projected DOS for the organic cations are added with shading.

Figure 4. Calculated transport coefficients for the organic-inorganic hybrid perovskite ABI_3 as a function of the chemical potential μ : (a) the Seebeck coefficients S, (b) the power factor $S^2\sigma$, (c) the electrical thermal conductivity κ_e, and (d) the figure of merit ZT. The filled triangles in (c) indicate the κ_e at the chemical potentials leading to the maximum ZTs, and the numbers at the peaks in (d) refer to the carrier concentrations (in units of 10^{19} cm^{-3}) at the chemical potentials leading to the maximum ZTs. The zero chemical potential refers to the midpoint of the band gap.

Table 1. Structural parameters and crystallographic data of ABI_3 taken from ref. 9.

	$(MA)PbI_3$	$(MA)SnI_3$	$(FA)PbI_3$	$(FA)SnI_3$
Crystal system	tetragonal	tetragonal	trigonal	orthorhombic
Space group	P4mm	P4mm	P3m1	Amm2
Unit cell Parameters (Å)	a=6.3115 b=6.3115 c=6.3161	a=6.2302 b=6.2302 c=6.2316	a=8.9817 b=8.9817 c=11.006	a=6.3286 b=8.9554 c=8.9463

Table 2. Calculated band gaps E_g (eV) of the perovskites ABI_3.

	$(MA)PbI_3$	$(FA)PbI_3$	$(MA)SnI_3$	$(FA)SnI_3$
GGA	1.69	1.62	0.86	0.74
GGA+SOC	1.12	0.91	0.78	0.75
Expt.	1.57 [34] 1.55 [34]	1.48 [35]	1.35 [7]	1.41[36]

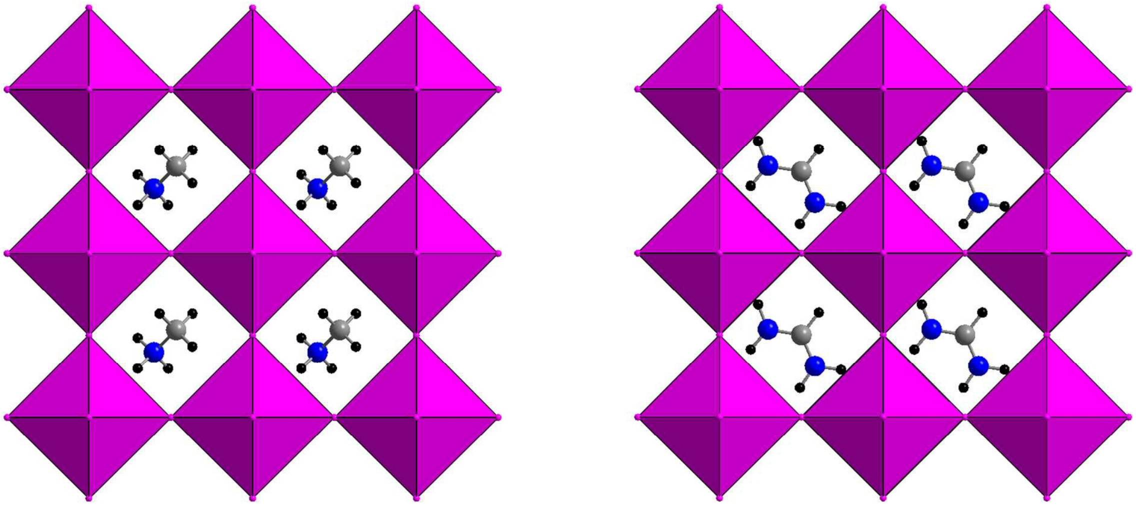

(a) (MA)BI_3 (b) (FA)BI_3

Figure 1.

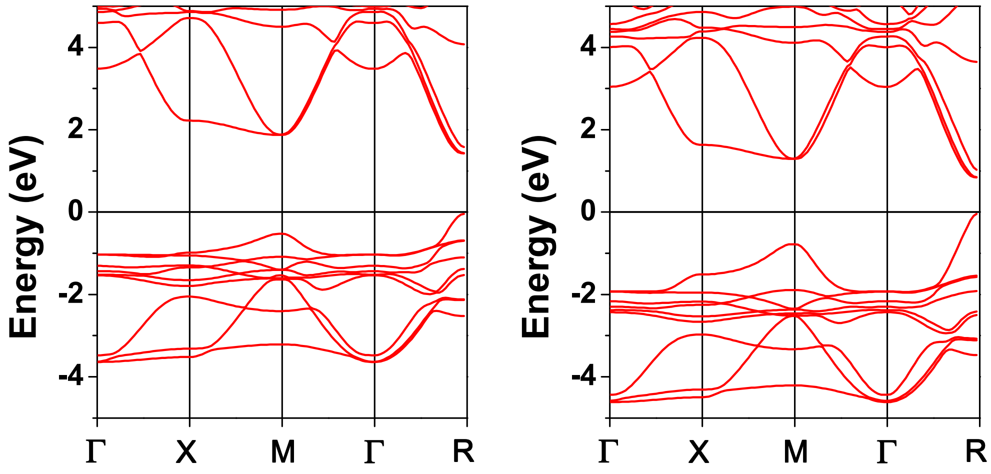

(a) (MA)PbI_3 (b) (MA)SnI_3

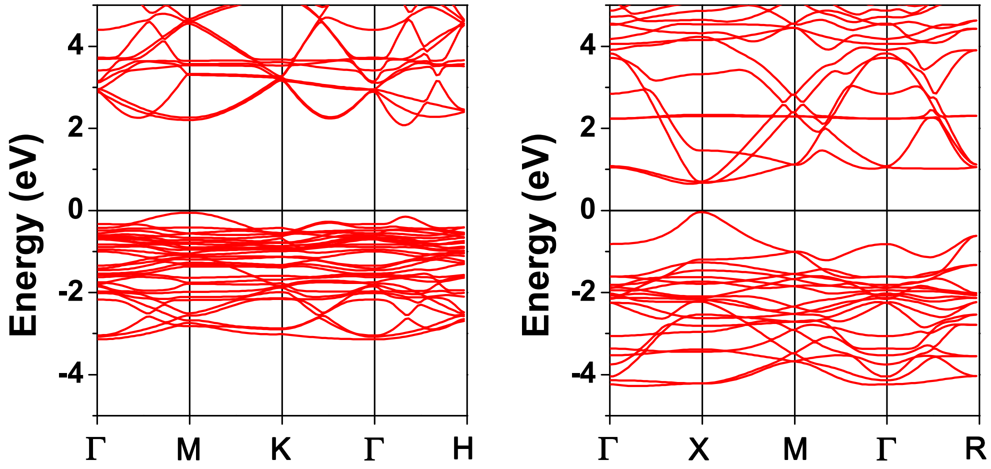

(c) (FA)PbI_3 (d) (FA)SnI_3

Figure 2

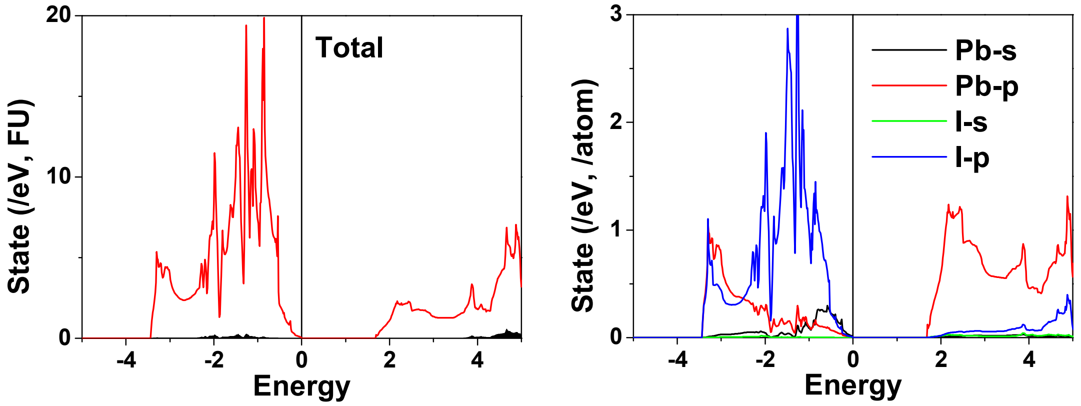

(a) (MA)PbI$_3$

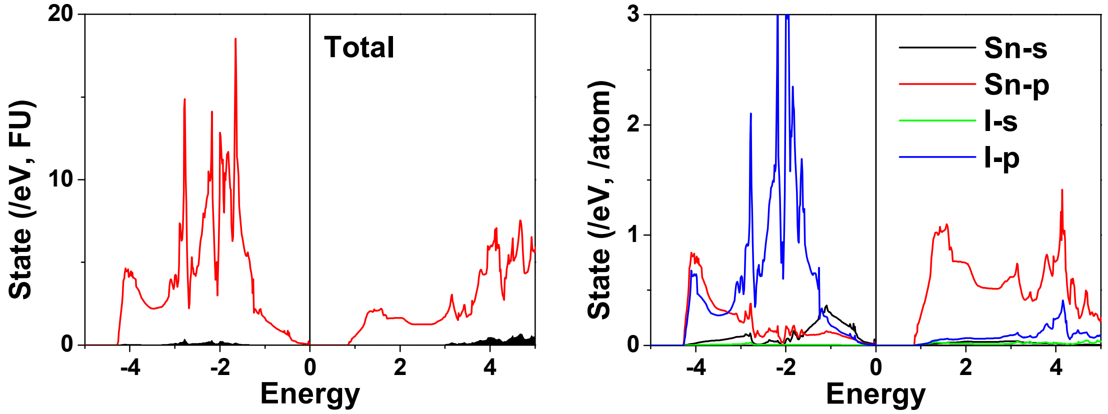

(b) (MA)SnI$_3$

Figure 3

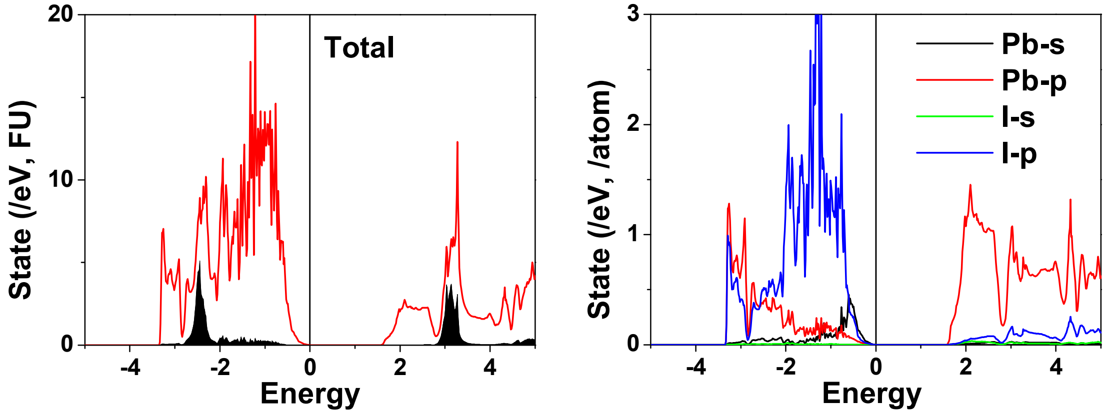

(c) (FA)PbI$_3$

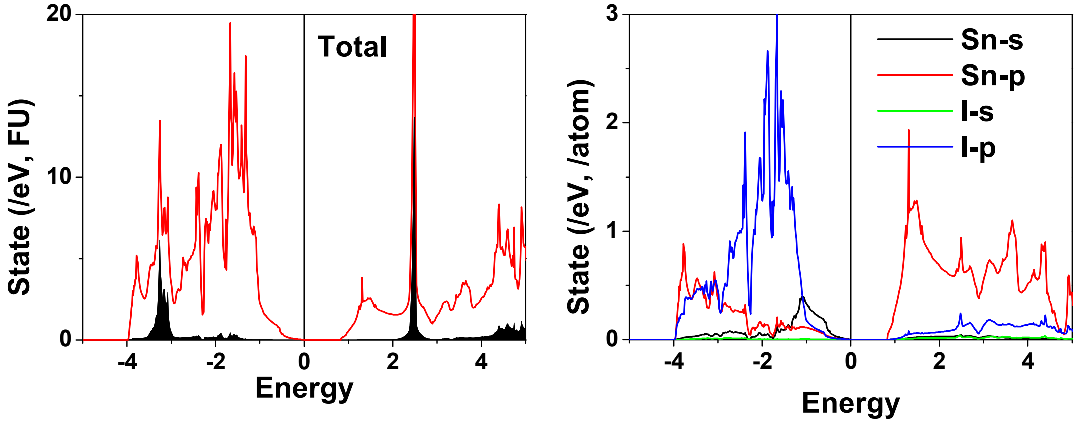

(d) (FA)SnI$_3$

Figure 3

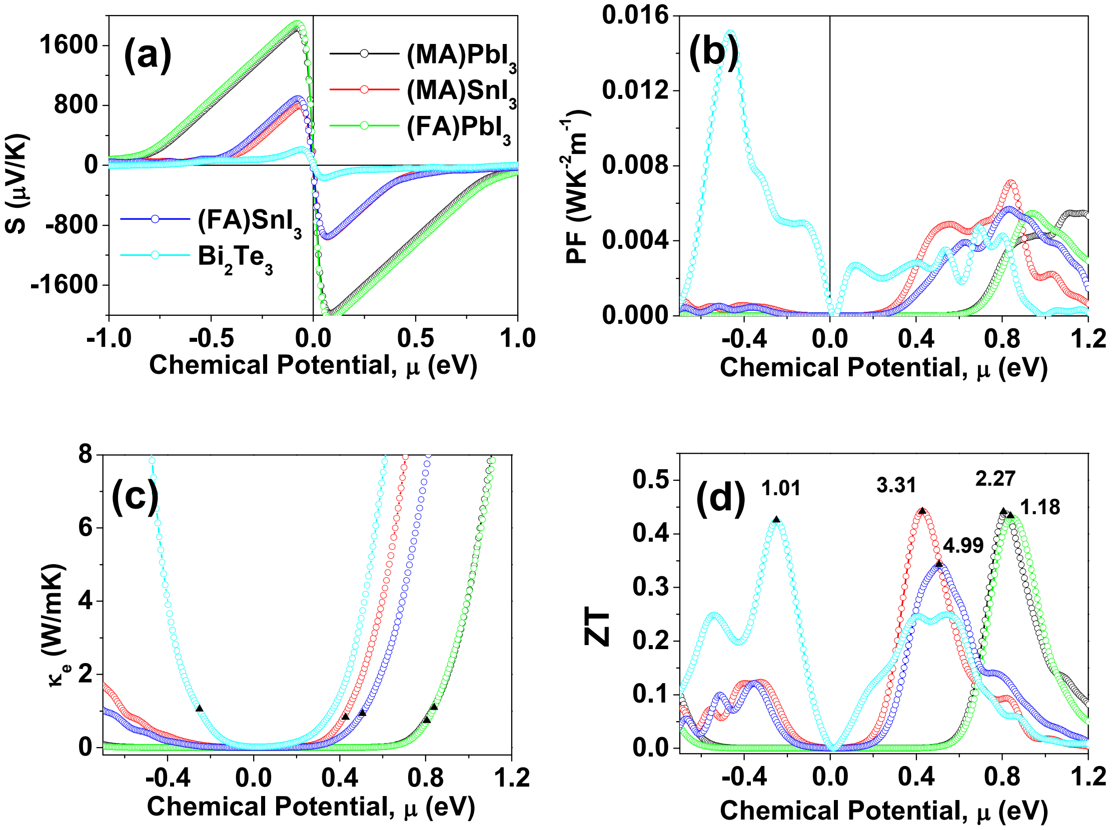
(a)
(MA)PbI3
(MA)SnI3
(FA)PbI3
(FA)SnI3
Bi2Te3
S (μV/K)
1600
800
0
-800
-1600
-1.0
-0.5
0.0
0.5
1.0
Chemical Potential, μ (eV)
(b)
PF (WK-2m-1)
0.016
0.012
0.008
0.004
0.000
-0.4
0.0
0.4
0.8
1.2
Chemical Potential, μ (eV)
(c)
κe (W/mK)
8
6
4
2
0
-0.4
0.0
0.4
0.8
1.2
Chemical Potential, μ (eV)
(d)
ZT
0.5
0.4
0.3
0.2
0.1
0.0
1.01
3.31
2.27
1.18
4.99
-0.4
0.0
0.4
0.8
1.2
Chemical Potential, μ (eV)

Figure 4